PHYSICS

Dynamics of correlation-frozen antinodal quasiparticles in superconducting cuprates

Federico Cilento,[1]* Giulia Manzoni,[1,2] Andrea Sterzi,[1,2] Simone Peli,[3] Andrea Ronchi,[3,4] Alberto Crepaldi,[5] Fabio Boschini,[6,7] Cephise Cacho,[8] Richard Chapman,[8] Emma Springate,[8] Hiroshi Eisaki,[9] Martin Greven,[10] Mona Berciu,[6,7] Alexander F. Kemper,[11] Andrea Damascelli,[6,7] Massimo Capone,[12] Claudio Giannetti,[3]* Fulvio Parmigiani[1,2,13]

Copyright © 2018 The Authors, some rights reserved; exclusive licensee American Association for the Advancement of Science. No claim to original U.S. Government Works. Distributed under a Creative Commons Attribution NonCommercial License 4.0 (CC BY-NC).

Many puzzling properties of high–critical temperature (T_c) superconducting (HTSC) copper oxides have deep roots in the nature of the antinodal quasiparticles, the elementary excitations with wave vector parallel to the Cu–O bonds. These electronic states are most affected by the onset of antiferromagnetic correlations and charge instabilities, and they host the maximum of the anisotropic superconducting gap and pseudogap. We use time-resolved extreme-ultraviolet photoemission with proper photon energy (18 eV) and time resolution (50 fs) to disclose the ultrafast dynamics of the antinodal states in a prototypical HTSC cuprate. After photoinducing a nonthermal charge redistribution within the Cu and O orbitals, we reveal a dramatic momentum-space differentiation of the transient electron dynamics. Whereas the nodal quasiparticle distribution is heated up as in a conventional metal, new quasiparticle states transiently emerge at the antinodes, similarly to what is expected for a photoexcited Mott insulator, where the frozen charges can be released by an impulsive excitation. This transient antinodal metallicity is mapped into the dynamics of the O-2p bands, thus directly demonstrating the intertwining between the low- and high-energy scales that is typical of correlated materials. Our results suggest that the correlation-driven freezing of the electrons moving along the Cu–O bonds, analogous to the Mott localization mechanism, constitutes the starting point for any model of high-T_c superconductivity and other exotic phases of HTSC cuprates.

INTRODUCTION

Many of the exotic phenomena characterizing the phase diagram of high–critical temperature (T_c) superconducting (HTSC) cuprates originate from the interplay between the Coulomb interactions within the Cu-3d orbitals and the tendency of holes to delocalize via the O-2p–mediated hopping (*1*, *2*). The redistribution of the charges within the Cu-O orbitals in doped materials drives the emergence of unconventional phenomena, such as the pseudogap phase (*3*, *4*), low-temperature charge instabilities (*2*, *5*), and d-wave superconductivity (*6*). A possible framework (*7*–*10*) to rationalize these phenomena relies on the assumption that, in lightly doped HTSC, the strong on-site repulsion drives the freezing of the electrons moving along the Cu–O bonds. The consequent breakdown of the Fermi surface (*11*), under the form of a suppression of quasiparticle excitations in the antinodal region of the Brillouin zone, prepares the emergence (*12*) of low-temperature instabilities and the opening of the d-wave superconducting gap. Within this picture, ultrafast resonant excitation can be used as an "unconventional" control parameter (*13*, *14*) to transiently modify the electronic occupancy of the Cu-3d and O-2p orbitals and drive the system toward a transient metallic state (*15*) characterized by the partial recovery of antinodal quasiparticle states at momenta $(\pm\pi,0)$ and $(0,\pm\pi)$.

Led by this idea, we performed high–temporal resolution extreme-ultraviolet (EUV) angle-resolved photoemission spectroscopy (TR-ARPES) to map the ultrafast evolution of both antinodal quasiparticles and O-2p bands in a prototypical cuprate superconductor (see Fig. 1, A to C, for an overview of the real- and momentum-space structure). Our experiment unveils an unconventional antinodal dynamics, characterized by the transient emergence of quasiparticle states, that is very similar to what is expected for a photoexcited Mott insulator. These results, supported by cluster dynamical mean-field theory (CDMFT) calculations within the single-band Hubbard model, suggest that the breakdown of the antinodal Fermi surface is a direct consequence of the short-range correlations induced by the on-site Coulomb repulsion. The ultrafast dynamics is triggered by near-infrared (1.65 eV) femtosecond pulses that excite the O-2p→Cu-3d charge-transfer process in $Bi_2Sr_2Ca_{0.92}Y_{0.08}Cu_2O_{8+\delta}$ (Y-Bi2212) single crystals close to the optimal hole concentration (T_c = 96 K).

RESULTS

Ultrafast photoexcitation in multiband copper oxides

To address the role of the oxygen bands in the photoexcitation process, we start from the one-hole solution (*16*) of the five-band model (Fig. 1), obtained from a generalized Emery model after projecting out the double occupancy of the Cu sites. The spectrum reveals the presence of two different oxygen bands at binding energies larger than 1 eV. The $2p_\sigma$ band has a maximum at momentum (0,0) and presents the same symmetry of the Cu-$3d_{x^2-y^2}$ states that give rise to the conduction band. In contrast, the $2p_\pi$ band, which arises from the hybridization of the

[1]Elettra-Sincrotrone Trieste S.C.p.A., 34149 Basovizza, Italy. [2]Dipartimento di Fisica, Università degli Studi di Trieste, 34127 Trieste, Italy. [3]Interdisciplinary Laboratories for Advanced Materials Physics, Università Cattolica del Sacro Cuore, I-25121 Brescia, Italy. [4]Department of Physics and Astronomy, Katholieke Universiteit Leuven, Celestijnenlaan 200D, 3001 Leuven, Belgium. [5]Institute of Physics, Ecole Polytechnique Fédérale de Lausanne, CH-1015 Lausanne, Switzerland. [6]Department of Physics and Astronomy, University of British Columbia, Vancouver, British Columbia V6T 1Z1, Canada. [7]Quantum Matter Institute, University of British Columbia, Vancouver, British Columbia V6T 1Z4, Canada. [8]CLF-Artemis@Rutherford Appleton Laboratory, Harwell Science and Innovation Campus, Didcot OX11 0QX, UK. [9]Nanoelectronics Research Institute, National Institute of Advanced Industrial Science Technology, Tsukuba, Ibaraki 305-8568, Japan. [10]School of Physics and Astronomy, University of Minnesota, Minneapolis, MN 55455, USA. [11]Department of Physics, North Carolina State University, Raleigh, NC 27695, USA. [12]Scuola Internazionale Superiore di Studi Avanzati (SISSA) and Consiglio Nazionale delle Ricerche–Istituto Officina dei Materiali (CNR-IOM) Democritos National Simulation Center, Via Bonomea 265, 34136 Trieste, Italy. [13]International Faculty, University of Cologne, Albertus-Magnus-Platz, 50923 Cologne, Germany.
*Corresponding author. Email: federico.cilento@elettra.eu (F.C.); claudio.giannetti@unicatt.it (C.G.)

Downloaded from http://advances.sciencemag.org/ on August 16, 2018

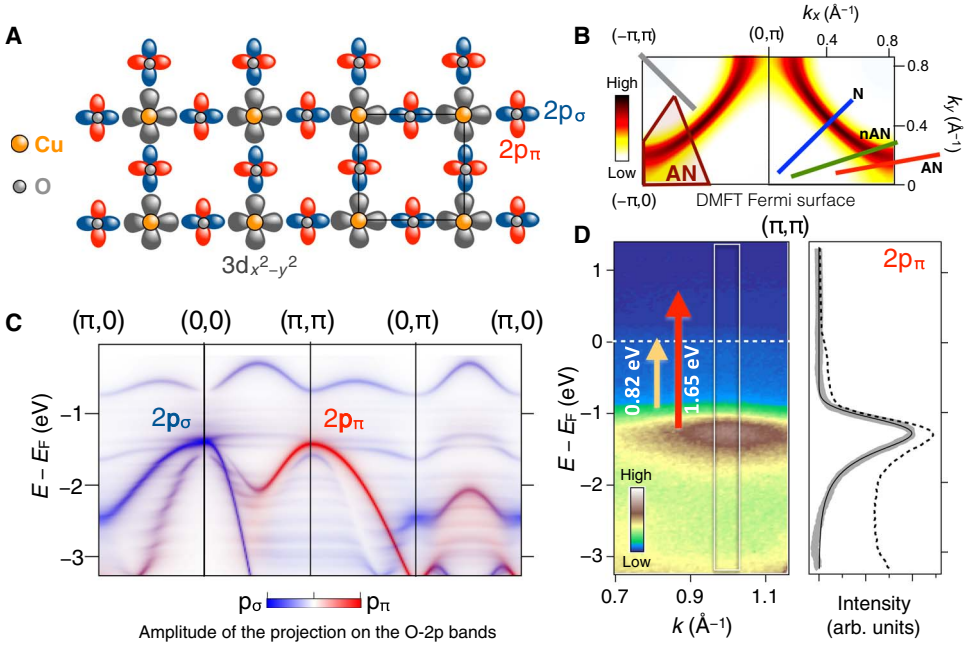

Fig. 1. Band structure of copper oxides. (**A**) Schematic representation of the Cu-3$d_{x^2-y^2}$ and the O-2$p_{x,y}$ orbitals that are included in the five-band model to reproduce the electronic band structure. (**B**) Upper half of the momentum-space unit cell (Brillouin zone). The Fermi surface is reconstructed by CDMFT (see Materials and Methods) for an optimally doped system. The red area indicates the antinodal region within the 4* patching of the Brillouin zone introduced by Gull *et al.* (*34*) for 2 × 2 CDMFT. The colored lines represent the nodal (N; blue), nearly antinodal (nAN; green), and antinodal (AN; red) cuts of the Brillouin zone accessible by photoemission with photon energy $\hbar\omega \approx 18$ eV and azimuthal angles $\theta_N = 0$, $\theta_{nAN} = 27°$, and $\theta_{AN} = 35°$. The gray line represents the cut along the (0,0)-(π,π) direction corresponding to the photoemission spectra from the O-2p_π band. (**C**) Band structure from the one-hole solution of the five-band generalized Emery model (see Materials and Methods). The color scale indicates the amplitude of the projection of the wave functions on the p_σ (blue) and p_π (red) orbitals. (**D**) The left panel displays the photoemission spectrum from the 2p_π oxygen bands at momentum (π,π). The color scale (arbitrary units) indicates the photoemission intensity. The arrows indicate the two different pumping schemes used in the experiments. The white rectangle highlights the area of integration for the EDCs reported in the right panel (dashed line). The peak attributed to the 2p_π band (gray line) is obtained by subtraction of an integral background. The black solid line is the result of the fit of an exponentially modified Gaussian curve to the EDC (see the Supplementary Materials).

O-2$p_{x,y}$ orbitals perpendicular to the O-2p ligand orbitals, has almost no overlap with the conduction band (see colors in Fig. 1C) and is observed as a strong photoemission peak (*17*, *18*) at momentum (π,π) and binding energy of ≈1.2 eV (Fig. 1D). These considerations suggest that the near-infrared (1.5-eV photon energy) excitation scheme, which is almost universally adopted in pump-probe experiments (*14*, *19*–*24*), is capable of modifying the equilibrium occupancy of the Cu (n_d) and O bands (n_σ,n_π), thus transferring a fraction $\delta n_d = -(\delta n_\sigma + \delta n_\pi)$ of charges from the oxygen to the copper orbitals.

Antinodal ultrafast dynamics

The dynamics of δn_d over the entire Brillouin zone is tracked by TR-ARPES (see Materials and Methods) in which the *s*-polarized probe photons ($\hbar\omega \approx 18$ eV) maintain (*25*) a temporal structure of the order of 50 fs (see Materials and Methods). In Fig. 2A, we report the band dispersion along the antinodal (AN) direction (Fig. 1B). Right after the excitation with fluence of 350 μJ/cm^2, the differential image, given by the difference between the pumped and unpumped ARPES images, shows an increase (red) of the counts above the Fermi level (E_F) accompanied by a decrease below E_F. The nature of this nonequilibrium distribution can be better appreciated by plotting (Fig. 2B) the differential energy distribution curves (EDCs) integrated in the momentum region highlighted by the black rectangle in Fig. 2A. The transient antinodal distribution is characterized by a strong electron-hole asymmetry, because the number of electrons above E_F significantly exceeds the number of photoexcited holes below E_F. This effect is maximum along the antinodal cut, whereas the differential signal along the nodal (N) direction is symmetric at all time scales. In Fig. 2C, we analyze the dynamics of the antinodal distribution by plotting the EDCs at different pump-probe delays. The EDCs are modeled as the product of a Fermi-Dirac distribution, $f(E,T_{eff})$, at the effective temperature T_{eff} and the spectral function $A(E) = \Sigma_2^2/\pi\left[(E - E_F - \Sigma_1)^2 + \Sigma_2^2\right]$, where $\Sigma = \Sigma_1 + i\Sigma_2$ is the electronic single-particle self-energy. The self-energy is phenomenologically modeled by the expression $\Sigma = i\Gamma + \Delta^2/(E - E_F + i\gamma_p)$, which is commonly adopted for gapped quasiparticles (*11*), where Γ is the quasiparticle scattering rate, Δ is the electron-hole symmetric pairing gap, and γ_p is a pair-breaking term. At negative delays, the EDCs (gray curve in Fig. 2C) are reproduced assuming an antinodal pseudogap $\Delta_{AN} = 40$ meV (*26*) and $T_{eff} = 30$ K, which corresponds to the temperature of the sample. In the first hundreds femtoseconds after the excitation (red curves), the EDCs are only partially reproduced by an increase of T_{eff} because they exhibit an excess signal (dashed area) above E_F, which is responsible for the asymmetry of the antinodal differential EDCs, as reported in Fig. 2B. The most notable result is that the asymmetry of the antinodal EDCs can be perfectly reproduced (see solid line in Fig. 2B) by assuming a net increase of states at the Fermi level, mimicked by adding a transient additional gapless spectral function, $\delta A_{AN}(E)$ (see the Supplementary Materials). We stress that a simple gap-filling/gap-closing process cannot account for the observed antinodal asymmetry. Any modification of a pairing gap, when convolved with the experimental resolution larger than the gap size, would give rise to a

Downloaded from http://advances.sciencemag.org/ on August 16, 2018

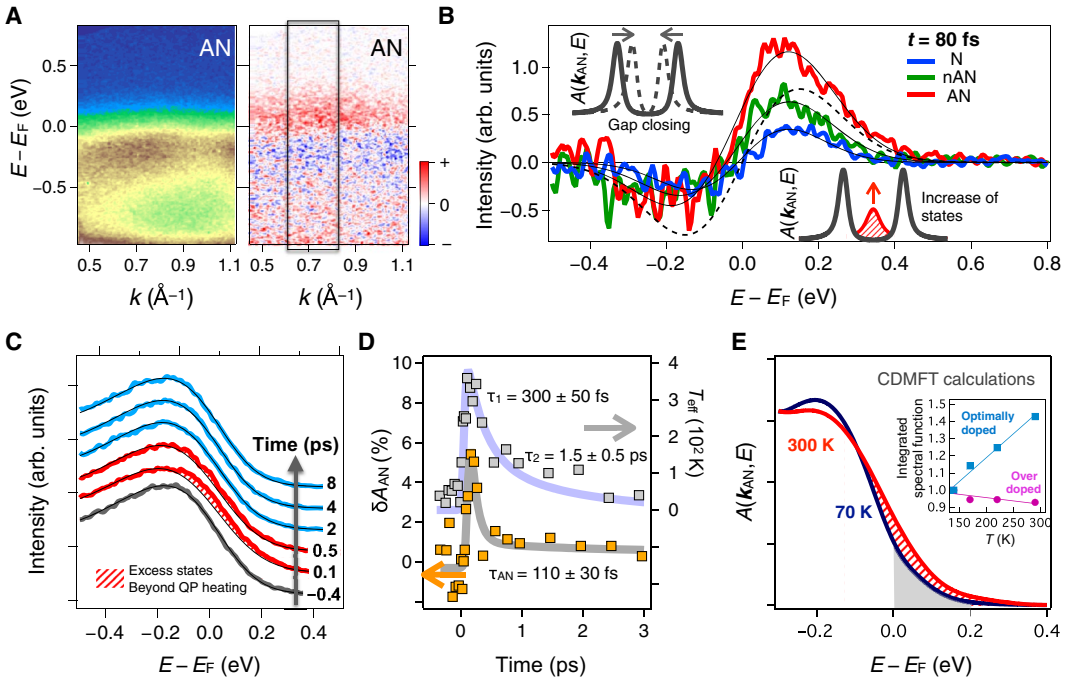

Fig. 2. Time-resolved photoemission spectra at the Fermi level. (**A**) Equilibrium (left) and differential (right) antinodal band dispersion. The differential spectrum is obtained as the difference between the pumped and unpumped ARPES images at fixed pump-probe delay (80 fs). The color scale of the differential spectrum highlights positive (red) and negative (blue) photoemission intensity variations. The black rectangle indicates the region of integration for the EDC curves shown in (B) and (C). (**B**) Differential EDC curves along the nodal, nearly antinodal, and antinodal directions. The black lines are the best fit to the nodal, nearly antinodal, and antinodal differential spectra, obtained by assuming a transient increase of the quasiparticle states and of the effective electronic temperature. The dashed line schematizes the symmetric signal expected for a gap closing/filling or a temperature increase. (**C**) Nonequilibrium EDC curves at different time delays. The dashed areas show the excess signal, with respect to a simple effective heating, related to the transient increase of states at the Fermi level. The colors highlight three different characteristic temporal regions corresponding to negative delays (gray trace), short dynamics characterized by the excess antinodal population (red traces), and long dynamics characterized by an increase of the electronic effective temperature (blue traces). The black lines show the effective temperature increase contribution to the total fit (see the Supplementary Materials), which also includes the variation of states at the Fermi level. QP, quasiparticle. (**D**) The dynamics of the antinodal increase of states (yellow squares, left axis), obtained by integrating the antinodal spectrum over the momentum-energy area indicated in (A), is reported. The gray line represents the best fit, which contains a single exponential decay with time constant $\tau_{AN} = 110 \pm 30$ fs. The effective temperature increase of the nodal Fermi-Dirac distribution (gray squares, right axis) is well reproduced by a double-exponential decay. The extracted time scales are in agreement with published results obtained in similar experimental conditions (*41*). (**E**) CDMFT solutions of the single-band Hubbard model for an optimally doped cuprate (see Materials and Methods). The lines represent the single-particle spectral functions in the antinodal region (Fig. 1B) at two different temperatures convolved with the experimental resolution. The inset shows the integral of the spectral function in the $0 < E - E_F < 0.2$ eV energy range (see gray area of the main panel) for optimally and overdoped materials (see Materials and Methods). The integrals have been normalized to the values at $T = 140$ K.

symmetric signal (see the Supplementary Materials) because the increase in the density of states at the Fermi level is compensated by a decrease of the states at the gap edge. In Fig. 2D, we report the dynamics of the antinodal ($0.6 < k < 0.8$ Å^{-1}) asymmetry, as obtained by integrating the photoemission intensity in the [−0.7,0.7] eV energy range. The data (yellow squares) show that the electron-hole asymmetry vanishes on a time scale of $\tau_{AN} = 110 \pm 30$ fs. This value is unrelated to the dynamics of T_{eff} (Fig. 2D), which can be estimated from the broadening of the nodal Fermi-Dirac distribution (see the Supplementary Materials). This finding suggests that the observed antinodal increase of states is not the simple result of a temperature-driven broadening of the electronic occupation of states that are intrinsically electron-hole asymmetric (*27*, *28*).

The nature of the antinodal states

Our observations indicate that the redistribution of a fraction of charges δn_d within the Cu-3d and O-2p oxygen bands induces transient new in-gap electronic states at the antinodes. This mechanism is very similar in nature to the collapse of the correlation gap in a photoexcited Mott insulator (*29*), which is determined by the formation of transient quasiparticle states whose spectral weight is compensated at an energy scale of few electron volts.

The observed dichotomy between the physics of "conventional" nodal quasiparticles and that of Mott-like antinodal excitations is a key consequence of the strong local correlations, as described at the most fundamental level by the single-band Hubbard model. To address the role of on-site correlations in determining the observed antinodal physics, we performed CDMFT calculations (see Materials and Methods), which capture the *k*-space differentiation of the elementary excitations close to the Fermi level. In Fig. 2E, we report the antinodal spectral function, convolved with the experimental resolution, at two different temperatures and for effective parameters that reproduce the physics of optimally and overdoped cuprates (see Materials and Methods). The calculations evidence a suppression of antinodal quasiparticles, which is progressively weakened as the energy of the system is raised under the form of a temperature increase. As a consequence, new states appear at the Fermi level, as can be appreciated by plotting the integral of $A(E)$ in the [0,0.2] eV

Downloaded from http://advances.sciencemag.org/ on August 16, 2018

range as a function of the temperature (see inset of Fig. 2E). As expected, this effect vanishes when the correlations are weakened by further increasing the hole concentration (see data for the overdoped system in the inset of Fig. 2E) up to the point of completely recovering a closed Fermi surface at all temperatures (*30*–*32*). Although the single-band Hubbard model cannot account for the details of the photoinduced charge redistribution within the Cu-O orbitals, it shows that the on-site Coulomb repulsion is the fundamental mechanism underlying the *k*-selective suppression of antinodal quasiparticles for doping concentrations as large as those corresponding to the maximal T_c (optimal doping). Furthermore, it correctly predicts the emergence of additional in-gap antinodal states when energy is provided to the system.

Ultrafast dynamics of the oxygen states

A more comprehensive picture of the relation between δn_d, δn_σ, and δn_π can be obtained by tracking the transient behavior of the O-2p bands after the O-2p→Cu-3d resonant excitation. In particular, we focus on the dynamics of the nonbonding O-2p_π band, which is observed as a strong asymmetric peak at momentum (π,π) (Fig. 1D). The position of this band is naturally linked to the occupancy of the Cu-3$d_{x^2-y^2}$ and O-2$p_{\pi,\sigma}$ bands. A simple mean-field calculation (see Materials and Methods) shows that the photoinduced change $\delta n_d = -(\delta n_\sigma + \delta n_\pi)$ of the orbital populations would induce a shift of the O-2p_π band energy given by

$$\delta\varepsilon_\pi \approx U_{pp}\left(\frac{1}{2}\delta n_\pi + \delta n_\sigma\right) + 2U_{pd}\delta n_d \quad (1)$$

where U_{pp} and U_{pd} are the Coulomb repulsions within oxygen sites and between the oxygen and copper orbitals, respectively. Equation 1 suggests that any spatially homogeneous combination of holes in the O-2p_π and O-2p_σ bands would give rise to an energy shift $\delta\varepsilon_\pi$. Considering the experimental fluence (see Materials and Methods) and the realistic values (*33*) U_{pp} = 5 eV and U_{pd} = 2 eV, we obtain, as lower and upper bounds, $\delta\varepsilon_\pi$ = −10 meV and +15 meV, corresponding to the cases in which the whole of the photons is absorbed via the creation of homogeneous δn_σ and δn_π distributions, respectively.

Figure 3A displays the differential spectra relative to the O-2p_π band for different pump-probe delays. In the first tens of femtoseconds, we observe a differential signal, which changes sign (positive, red; negative,

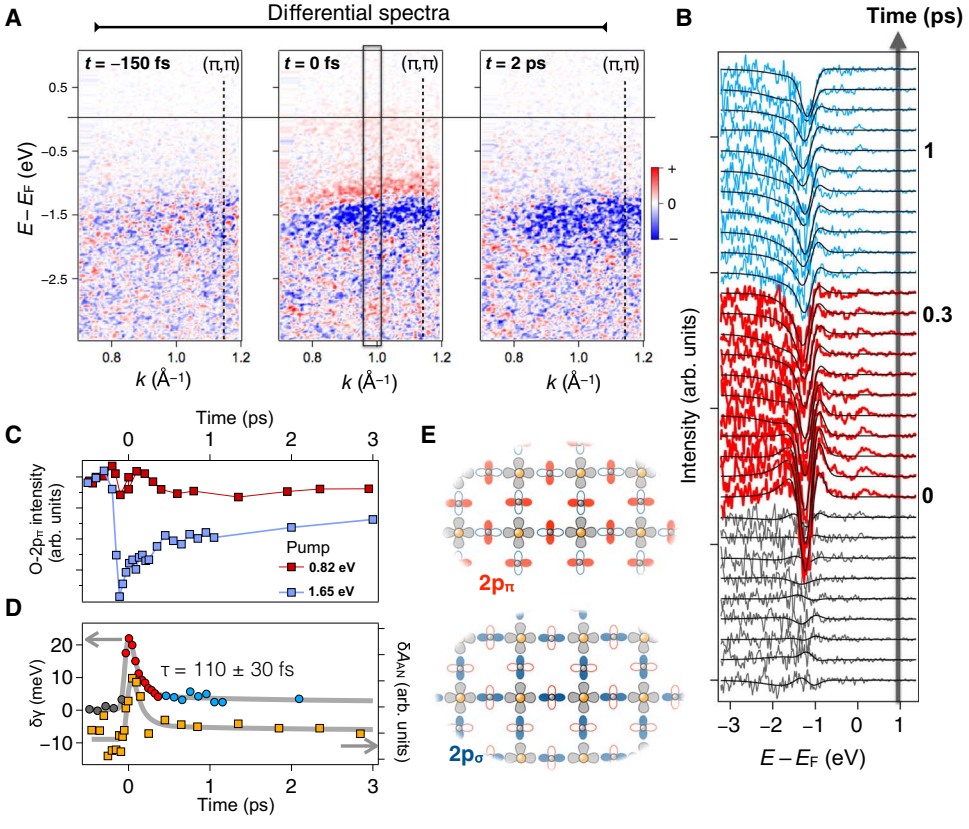

Fig. 3. Time-resolved photoemission spectra of the oxygen bands. (**A**) Differential ARPES spectra in the (π,π) momentum region at different time delays. The color scale highlights positive (red) and negative (blue) photoemission intensity variations. The black rectangle indicates the region of integration for the EDC curves shown in (B). (**B**) Differential EDC curves as a function of the time delay. The colors highlight three different characteristic temporal regions corresponding to negative delays (gray traces), short dynamics characterized by a transient broadening of the O-2p_π peak (red traces), and long dynamics characterized by a long-lived decrease of the O-2p_π peak spectral weight. The black lines are the differential fit to the data obtained by assuming both a Gaussian broadening and a spectral weight decrease of the O-2p_π. (**C**) Dynamics of the photoemission intensity at a binding energy of 1.2 eV for the 0.82-eV (red squares) and 1.65-eV (blue squares) pump excitations. (**D**) Dynamics of the O-2p_π peak broadening (circles, left axis). The colors represent the three different time scales shown in (B). For the sake of comparison, we show the antinodal increase of states (yellow squares, right axis), already reported in Fig. 2D. (**E**) Cartoon of the inhomogeneous (in real space) excitation pattern of the O-2p_π and O-2p_σ orbitals at very short time scales (0 to 300 fs).

Downloaded from http://advances.sciencemag.org/ on August 16, 2018

blue) at the energy corresponding to the binding energy of the O-2p_π levels. At longer times, the differential signal is characterized by a homogeneous negative variation. The quantitative analysis of this dynamics is reported in Fig. 3B. The differential EDCs are fitted by modifying the smallest number of parameters in the exponentially broadened Gaussian function (see the Supplementary Materials) that reproduces the equilibrium peak shape reported in Fig. 1D. In particular, the signal is reproduced over the entire time scale by assuming (i) a long-lived spectral weight variation and (ii) an additional transient Gaussian broadening, $\delta\gamma$, which adds to an equilibrium broadening of $\gamma \approx 160$ meV, corresponding to the energy resolution of the experiment. The position of the O-2p_π peak remains always constant during the time evolution, in contrast to what is expected for a homogeneous distribution of δn_σ and δn_π excitations (Eq. 1).

In Fig. 3D, we report the temporal evolution of $\delta\gamma$. The maximum amplitude of the transient broadening roughly corresponds to the energy difference (≈25 meV) between the energy shifts expected for the homogeneous excitation of the O-2p_σ and O-2p_π bands. The natural explanation of this result is that the transient increase of the population in the conduction band, δn_d, is associated with the formation of a spatially inhomogeneous pattern of excess holes involving either the π or the σ oxygen bands (Fig. 3E). This situation gives rise to a Gaussian distribution of $\delta\varepsilon_\pi$ reflecting the statistical spatial distribution of the possible mixtures of δn_π and δn_σ excitations. This picture is supported by the comparison between the dynamics of $\delta\gamma$ and that of the antinodal excess population, as shown in Fig. 3D. The Gaussian broadening of the O-2p_π peak recovers its resolution-limited value on a time scale identical to the relaxation time of the excess population (τ_{AN}) measured at the antinode and shown in Fig. 2.

As a final proof of the relation between the observed broadening and the creation of a nonthermal charge distribution in the Cu-3d and O-2p bands, we repeated the same experiment with a pump excitation characterized by the same absorbed fluence but a photon energy ($\hbar\omega$ = 0.82 eV) smaller than that necessary to transfer electrons from the O-2$p_{\sigma,\pi}$ bands to the Cu-3$d_{x^2-y^2}$ conduction band. As shown in Fig. 3C, no dynamics of the O-2p_π is observed in the case of off-resonant excitation, thus ruling out thermal heating effects as the origin of the observed phenomena.

DISCUSSION

Our experiment demonstrates that the suppression of quasiparticle states at the antinodes is originated by a correlation-driven breakup of the Fermi surface, as already suggested by DMFT calculations for the single-band Hubbard model (*7*, *8*, *10*, *34*). In this framework, the photoexcitation drives the evolution of antinodal states from Mott-like gapped excitations to delocalized quasiparticles, as previously suggested by all optical experiments (*15*). The present results directly affect the current knowledge of the physics of cuprate superconductors. Any model for explaining the d-wave superconducting pairing, the antinodal pseudogap, and the fragility toward charge ordering should build on a ground state in which the strong on-site Coulomb repulsion drives the freezing of antinodal quasiparticles. Finally, although the resonant optical excitation is spatially homogeneous, it likely gives rise to an inhomogeneous pattern of δn_π and δn_σ distributions. Whether this is the consequence of the spontaneous and ultrafast segregation of charges in the O-2$p_{\sigma,\pi}$ bands or it reflects an underlying inhomogeneity of the oxygens (*5*, *35*–*37*) remains an open fascinating question that requires further investigation.

More generally, the possibility of manipulating the orbital occupancy offers a new way to control the transient properties in correlated and multiorbital materials and to achieve novel functionalities, such as the photoinduced antinodal metallicity shown in this work. The complete reconstruction of the *k*-space dynamics of the conduction band and of the high–binding energy states demonstrated here will constitute the cornerstone for the next generation of experiments based on the novel EUV ultrafast sources that are currently being developed. Our results also constitute the benchmark for future realistic models of the band structure dynamics of multiband correlated materials, in which the orbital occupation can be manipulated on demand by light.

MATERIALS AND METHODS

Experimental design

Time-resolved ARPES measurements were performed at the Materials Science end-station at the Artemis facility (Central Laser Facility, Rutherford Appleton Laboratory). The facility is equipped with a 1-kHz Ti:sapphire amplified laser system delivering ≈30-fs pulses with a central wavelength of 790 nm. The EUV probe photons (in the range of 15 to 40 eV) are produced by high-harmonic generation (HHG) in an argon gas jet. The *s*-polarized 11th harmonics at ≈18 eV was selected through a time-preserving monochromator (exploiting gratings mounted in the off-plane geometry to preserve the short temporal duration of the pulses). The EDCs reported in Figs. 1 to 3 were fitted by convolving the appropriate fit function with a Gaussian function, which accounts for the experimental energy resolution. The Gaussian full width at half maximum is 250 meV for the measurements performed close to the Fermi level and 160 meV for the measurements of the oxygen bands. These values correspond to the different settings of the exit slit of the monochromator of the HHG beamline, optimized for obtaining the best compromise between photon flux and energy resolution.

The nodal, nearly antinodal, and antinodal cuts of the Fermi surface reported in Fig. 2 were obtained by rotating the sample around its azimuthal plane. The sample alignment was determined ex situ by Laue diffraction and checked in situ by low-energy electron diffraction technique. The pump beam was generated using a high-energy optical parametric amplifier and tuned to 1510 nm (0.82 eV). For quasiresonant excitation, the second harmonics of this photon energy was generated in a thin (0.1 mm) phase-matched BBO crystal, thus obtaining a beam at 755 nm (1.65 eV). Both beams were *s*-polarized. The overall temporal resolution in the pump-probe experiments was <50 fs. The density of excited Cu atoms can be calculated considering the pump energy density (25 J/cm^3) and the density of Cu atoms (1.3×10^{-22} cm^{-3}). The fraction of excited Cu atoms is thus 0.01.

Band structure calculations

The five-band model we used to calculate the spectrum shown in Fig. 1C is explained by Ebrahimnejad *et al.* (*16*). These results are generated with the same variational method used there to calculate the quasiparticle band, which hosts the Fermi level upon doping (the highest energy band shown in Fig. 1C). Although the position and bandwidth of this band were found to depend on the variational space used, specifically on the maximum number of magnons allowed into the quasiparticle cloud, the O bands, especially the 2p_π one, are very robust and insensitive to such details. This fact further illustrates the lack of hybridization between these bands.

Downloaded from http://advances.sciencemag.org/ on August 16, 2018

Dynamical mean-field theory calculations

The Hubbard model has been solved by means of CDMFT that maps the full lattice model onto a finite small cluster (here, a four-site cluster) embedded in an effective medium that is self-consistently determined as in standard mean-field theory. The method therefore fully accounts for the short-range quantum correlations inside the cluster. The calculations use the dynamical cluster approximation prescription (*38*) and the 4* patching of the Brillouin zone introduced by Gull *et al.* (*34*) and have been performed using finite-temperature exact diagonalization (*39*) to solve the self-consistent cluster problem using eight energy levels in the bath as in several previous calculations. The finite-temperature version of the exact diagonalization has been implemented as discussed by Gull *et al.* (*34*) including typically 40 states in the low-temperature expansion of the observables. It is well established that CDMFT calculations with small cluster sizes reproduce the qualitative phase diagram of cuprates at doping smaller than the experimental ones. This discrepancy depends on the details of the calculations [see the study of Gull *et al.* (*40*)]. For the CDMFT parameters used in this work, the properties corresponding to optimally doped materials are obtained at a nominal hole concentration of $P = 0.09$. The properties typical of overdoped materials are obtained at $P = 0.2$.

Mean-field estimation of the oxygen orbitals energy

We considered the interaction piece of the five-orbital Emery-Hubbard model with on-site and nearest-neighbor interactions on the basis of Cu-3d$_{x^2-y^2}$ and O-2p$_{x,y}$ orbitals:

$$H(\mathbf{r}) = \sum_{\alpha}\left[(\varepsilon_{\mathrm{d}}-\mu)n_{\mathrm{d}}^{\alpha}(\mathbf{r}) + (\varepsilon_{\sigma}-\mu)n_{\sigma}^{\alpha}(\mathbf{r}) + (\varepsilon_{\pi}-\mu)n_{\pi}^{\alpha}(\mathbf{r})\right]$$
$$+ U_{\mathrm{dd}}n_{\mathrm{d}}^{\uparrow}(\mathbf{r})n_{\mathrm{d}}^{\downarrow}(\mathbf{r}) + \sum_{\alpha,\alpha'}U_{\mathrm{pd}}n_{\mathrm{p}}^{\alpha}(\mathbf{r})n_{\mathrm{d}}^{\alpha'}(\mathbf{r})$$
$$+ U_{\mathrm{pp}}\left[n_{\sigma}^{\uparrow}(\mathbf{r})n_{\sigma}^{\downarrow}(\mathbf{r}) + n_{\pi}^{\uparrow}(\mathbf{r})n_{\pi}^{\downarrow}(\mathbf{r})\right]$$
$$+ \sum_{\alpha,\alpha'}(U_{\mathrm{pp}}-2J_{\mathrm{pp}})n_{\sigma}^{\alpha}(\mathbf{r})n_{\pi}^{\alpha'}(\mathbf{r})$$

where n_{d}, n_{σ}, and n_{π} are the occupations of the Cu-3d, O-2p$_{\sigma}$, and O-2p$_{\pi}$ orbitals, and $n_{\mathrm{p}} = n_{\sigma} + n_{\pi}$. U_{dd} and U_{pp} are the on-site Coulomb interaction for the Cu-3d and O-2p orbitals, and U_{pd} is the intersite interaction. For the interaction $U_{\mathrm{p'p}}$ between the p$_{\pi}$ and p$_{\sigma}$ orbitals, we assumed spin-rotation invariance: $U_{\mathrm{p'p}} = U_{\mathrm{pp}} - 2J_{\mathrm{pp}}$.

We performed a mean-field decomposition in the absence of any magnetization ($n^{\uparrow} = n^{\downarrow}$) and obtained the following renormalizations of the on-site energy for the p$_{\pi}$ and p$_{\sigma}$ orbitals

$$\delta\varepsilon_{\pi} \approx U_{\mathrm{pp}}\left(\frac{1}{2}\delta n_{\pi} + \delta n_{\sigma}\right) + 2U_{\mathrm{pd}}\delta n_{\mathrm{d}} - 2J_{\mathrm{pp}}\delta n_{\sigma}$$
$$\delta\varepsilon_{\sigma} \approx U_{\mathrm{pp}}\left(\frac{1}{2}\delta n_{\sigma} + \delta n_{\pi}\right) + 2U_{\mathrm{pd}}\delta n_{\mathrm{d}} - 2J_{\mathrm{pp}}\delta n_{\pi}$$

SUPPLEMENTARY MATERIALS

Supplementary material for this article is available at http://advances.sciencemag.org/cgi/content/full/4/2/eaar1998/DC1

section S1. EDCs at equilibrium and effective temperature dynamics
section S2. Transient modification of photoemission intensity at $E \approx E_{\mathrm{F}}$
section S3. Transient broadening of the O-2p$_{\pi}$ band
fig. S1. Equilibrium EDCs.
fig. S2. Nonequilibrium EDCs.
fig. S3. Simulations of differential EDCs.
References (*42*, *43*)

REFERENCES AND NOTES

1. P. A. Lee, N. Nagaosa, X.-G. Wen, Doping a Mott insulator: Physics of high-temperature superconductivity. *Rev. Mod. Phys.* **78**, 17–85 (2006).
2. B. Keimer, S. A. Kivelson, M. R. Norman, S. Uchida, J. Zaanen, From quantum matter to high-temperature superconductivity in copper oxides. *Nature* **518**, 179–186 (2015).
3. T. Timusk, B. Statt, The pseudogap in high-temperature superconductors: An experimental survey. *Rep. Prog. Phys.* **62**, 61–122 (1999).
4. M. Norman, D. Pines, C. Kallin, The pseudogap: Friend or foe of high T_c. *Adv. Phys.* **54**, 715–733 (2005).
5. E. Fradkin, S. Kivelson, High-temperature superconductivity: Ineluctable complexity. *Nat. Phys.* **8**, 864–866 (2012).
6. C. C. Tsuei, J. R. Kirtley, Pairing symmetry in cuprate superconductors. *Rev. Mod. Phys.* **72**, 969–1016 (2000).
7. M. Civelli, M. Capone, S. S. Kancharla, O. Parcollet, G. Kotliar, Dynamical breakup of the Fermi surface in a doped Mott insulator. *Phys. Rev. Lett.* **95**, 106402 (2005).
8. M. Ferrero, P. S. Cornaglia, L. De Leo, O. Parcollet, G. Kotliar, A. Georges, Pseudogap opening and formation of Fermi arcs as an orbital-selective Mott transition in momentum space. *Phys. Rev. B* **80**, 064501 (2009).
9. T. Rice, K.-Y. Yang, F. Zhang, A phenomenological theory of the anomalous pseudogap phase in underdoped cuprates. *Rep. Prog. Phys.* **75**, 016502 (2012).
10. H. Alloul, What is the simplest model that captures the basic experimental facts of the physics of underdoped cuprates? *C. R. Phys.* **15**, 519–524 (2014).
11. M. R. Norman, M. Randeria, H. Ding, J. C. Campuzano, Phenomenology of the low-energy spectral function in high-T_c superconductors. *Phys. Rev. B* **57**, R11093 (1998).
12. S. Peli, S. Dal Conte, R. Comin, N. Nembrini, A. Ronchi, P. Abrami, F. Banfi, G. Ferrini, D. Brida, S. Lupi, M. Fabrizio, A. Damascelli, M. Capone, G. Cerullo, C. Giannetti, Mottness at finite doping and charge-instabilities in cuprates. *Nat. Phys.* **13**, 806–811 (2017).
13. J. Orenstein, Ultrafast spectroscopy of quantum materials. *Phys. Today* **65**, 44–50 (2012).
14. C. Giannetti, M. Capone, D. Fausti, M. Fabrizio, F. Parmigiani, D. Mihailovic, Ultrafast optical spectroscopy of strongly correlated materials and high-temperature superconductors: A non-equilibrium approach. *Adv. Phys.* **65**, 58–238 (2016).
15. F. Cilento, S. Dal Conte, G. Coslovich, S. Peli, N. Nembrini, S. Mor, F. Banfi, G. Ferrini, H. Eisaki, M. K. Chan, C. J. Dorow, M. J. Veit, M. Greven, D. van der Marel, R. Comin, A. Damascelli, L. Rettig, U. Bovensiepen, M. Capone, C. Giannetti, F. Parmigiani, Photo-enhanced antinodal conductivity in the pseudogap state of high-T_c cuprates. *Nat. Commun.* **5**, 4353 (2014).
16. H. Ebrahimnejad, G. A. Sawatzky, M. Berciu, The dynamics of a doped hole in a cuprate is not controlled by spin fluctuations. *Nat. Phys.* **10**, 951–955 (2014).
17. K. M. Shen, F. Ronning, D. H. Lu, W. S. Lee, N. J. C. Ingle, W. Meevasana, F. Baumberger, A. Damascelli, N. P. Armitage, L. L. Miller, Y. Kohsaka, M. Azuma, M. Takano, H. Takagi, Z.-X. Shen, Missing quasiparticles and the chemical potential puzzle in the doping evolution of the cuprate superconductors. *Phys. Rev. Lett.* **93**, 267002 (2004).
18. K. M. Shen, F. Ronning, W. Meevasana, D. H. Lu, N. J. C. Ingle, F. Baumberger, W. S. Lee, L. L. Miller, Y. Kohsaka, M. Azuma, M. Takano, H. Takagi, Z.-X. Shen, Angle-resolved photoemission studies of lattice polaron formation in the cuprate $Ca_2CuO_2Cl_2$. *Phys. Rev. B* **75**, 075115 (2007).
19. L. Perfetti, P. A. Loukakos, M. Lisowski, U. Bovensiepen, H. Eisaki, M. Wolf, Ultrafast electron relaxation in superconducting $Bi_2Sr_2CaCu_2O_{8+\delta}$ by time-resolved photoelectron spectroscopy. *Phys. Rev. Lett.* **99**, 197001 (2007).
20. J. Graf, C. Jozwiak, C. L. Smallwood, H. Eisaki, R. A. Kaindl, D.-H. Lee, A. Lanzara, Nodal quasiparticle meltdown in ultrahigh-resolution pump–probe angle-resolved photoemission. *Nat. Phys.* **7**, 805–809 (2011).
21. C. L. Smallwood, J. P. Hinton, C. Jozwiak, W. Zhang, J. D. Koralek, H. Eisaki, D.-H. Lee, J. Orenstein, A. Lanzara, Tracking cooper pairs in a cuprate superconductor by ultrafast angle-resolved photoemission. *Science* **336**, 1137–1139 (2012).
22. G. L. Dakovski, T. Durakiewicz, J.-X. Zhu, P. S. Riseborough, G. Gu, S. M. Gilbertson, A. Taylor, G. Rodriguez, Quasiparticle dynamics across the full Brillouin zone of $Bi_2Sr_2CaCu_2O_{8+\delta}$ traced with ultrafast time and angle-resolved photoemission spectroscopy. *Struct. Dyn.* **2**, 054501 (2015).
23. Y. Ishida, T. Saitoh, T. Mochiku, T. Nakane, K. Hirata, S. Shin, Quasi-particles ultrafastly releasing kink bosons to form Fermi arcs in a cuprate superconductor. *Sci. Rep.* **6**, 18747 (2016).

Downloaded from http://advances.sciencemag.org/ on August 16, 2018

24. J. D. Rameau, S. Freutel, A. F. Kemper, M. A. Sentef, J. K. Freericks, I. Avigo, M. Ligges, L. Rettig, Y. Yoshida, H. Eisaki, J. Schneeloch, R. D. Zhong, Z. J. Xu, G. D. Gu, P. D. Johnson, U. Bovensiepen, Energy dissipation from a correlated system driven out of equilibrium. *Nat. Commun.* **7**, 13761 (2016).
25. F. Frassetto, C. Cacho, C. A. Froud, E. I. Turcu, P. Villoresi, W. A. Bryan, E. Springate, L. Poletto, Single-grating monochromator for extreme-ultraviolet ultrashort pulses. *Opt. Express* **19**, 19169–19181 (2011).
26. W. S. Lee, I. M. Vishik, K. Tanaka, D. H. Lu, T. Sasagawa, N. Nagaosa, T. P. Devereaux, Z. Hussain, Z.-X. Shen, Abrupt onset of a second energy gap at the superconducting transition of underdoped Bi2212. *Nature* **450**, 81–84 (2007).
27. M. Hashimoto, R.-H. He, K. Tanaka, J.-P. Testaud, W. Meevasana, R. G. Moore, D. Lu, H. Yao, Y. Yoshida, H. Eisaki, T. P. Devereaux, Z. Hussain, Z.-X. Shen, Particle–hole symmetry breaking in the pseudogap state of Bi2201. *Nat. Phys.* **6**, 414–418 (2010).
28. T. L. Miller, W. Zhang, H. Eisaki, A. Lanzara, Particle-hole asymmetry in the cuprate pseudogap measured with time-resolved spectroscopy. *Phys. Rev. Lett.* **118**, 097001 (2017).
29. L. Perfetti, P. A. Loukakos, M. Lisowski, U. Bovensiepen, H. Berger, S. Biermann, P. S. Cornaglia, A. Georges, M. Wolf, Time evolution of the electronic structure of 1*T*-TaS_2 through the insulator-metal transition. *Phys. Rev. Lett.* **97**, 067402 (2006).
30. M. Platé, J. D. F. Mottershead, I. S. Elfimov, D. C. Peets, R. Liang, D. A. Bonn, W. N. Hardy, S. Chiuzbaian, M. Falub, M. Shi, L. Patthey, A. Damascelli, Fermi surface and quasiparticle excitations of overdoped $Tl_2Ba_2CuO_{6+\delta}$. *Phys. Rev. Lett.* **95**, 077001 (2005).
31. K. Fujita, C. K. Kim, I. Lee, J. Lee, M. H. Hamidian, I. A. Firmo, S. Mukhopadhyay, H. Eisaki, S. Uchida, M. J. Lawler, E.-A. Kim, J. C. Davis, Simultaneous transitions in cuprate momentum-space topology and electronic symmetry breaking. *Science* **344**, 612–616 (2014).
32. Y. He, Y. Yin, M. Zech, A. Soumyanarayanan, M. M. Yee, T. Williams, M. C. Boyer, K. Chatterjee, W. D. Wise, I. Zeljkovic, T. Kondo, T. Takeuchi, H. Ikuta, P. Mistark, R. S. Markiewicz, A. Bansil, S. Sachdev, E. W. Hudson, J. E. Hoffman, Fermi surface and pseudogap evolution in a cuprate superconductor. *Science* **344**, 608–611 (2014).
33. P. Hansmann, N. Parragh, A. Toschi, G. Sangiovanni, K. Held, Importance of *d-p* Coulomb interaction for high T_c cuprates and other oxides. *New J. Phys.* **16**, 033009 (2014).
34. E. Gull, M. Ferrero, O. Parcollet, A. Georges, A. J. Millis, Momentum-space anisotropy and pseudogaps: A comparative cluster dynamical mean-field analysis of the doping-driven metal-insulator transition in the two-dimensional Hubbard model. *Phys. Rev. B* **82**, 155101 (2010).
35. S. H. Pan, J. P. O'Neal, R. L. Badzey, C. Chamon, H. Ding, J. R. Engelbrecht, Z. Wang, H. Eisaki, S. Uchida, A. K. Guptak, K.-W. Ng, E. W. Hudson, K. M. Lang, J. C. Davis, Microscopic electronic inhomogeneity in the high-T_c superconductor $Bi_2Sr_2CaCu_2O_{8+x}$. *Nature* **413**, 282–285 (2001).
36. J. W. Alldredge, K. Fujita, H. Eisaki, S. Uchida, K. McElroy, Universal disorder in $Bi_2Sr_2CaCu_2O_{8+x}$. *Phys. Rev. B* **87**, 104520 (2013).
37. G. Campi, A. Bianconi, N. Poccia, G. Bianconi, L. Barba, G. Arrighetti, D. Innocenti, J. Karpinski, N. Zhigadlo, S. Kazakov, M. Burghammer, M. v. Zimmermann, M. Sprung, A. Ricci, Inhomogeneity of charge-density-wave order and quenched disorder in a high-T_c superconductor. *Nature* **525**, 359–362 (2015).
38. T. Maier, M. Jarrell, T. Pruschke, M. H. Hettler, Quantum cluster theories. *Rev. Mod. Phys.* **77**, 1027 (2005).
39. M. Capone, L. de' Medici, A. Georges, Solving the dynamical mean-field theory at very low temperatures using the Lanczos exact diagonalization. *Phys. Rev. B* **76**, 245116 (2007).
40. E. Gull, O. Parcollet, A. J. Millis, Superconductivity and the pseudogap in the two-dimensional Hubbard model. *Phys. Rev. Lett.* **110**, 216405 (2013).
41. C. L. Smallwood, W. Zhang, T. L. Miller, G. Affeldt, K. Kurashima, C. Jozwiak, T. Noji, Y. Koike, H. Eisaki, D.-H. Lee, R. A. Kaindl, A. Lanzara, Influence of optically quenched superconductivity on quasiparticle relaxation rates in $Bi_2Sr_2CaCu_2O_{8+\delta}$. *Phys. Rev. B* **92**, 161102 (2015).
42. O. N. Torrens, M. Zheng, J. M. Kikkawa, Energy of *K*-momentum dark excitons in carbon nanotubes by optical spectroscopy. *Phys. Rev. Lett.* **101**, 157401 (2008).
43. R. Matsunaga, K. Matsuda, Y. Kanemitsu, Origin of low-energy photoluminescence peaks in single carbon nanotubes: K-momentum dark excitons and triplet dark excitons. *Phys. Rev. B* **81**, 033401 (2010).

Acknowledgments

Funding: C.G. acknowledges support from Università Cattolica del Sacro Cuore through D1, D.2.2, and D.3.1 grants. M.C. and C.G. acknowledge financial support from the Italian Instruction, University and Research Ministry through the Research Projects of Relevant National Interest 2015 program (Prot. 2015C5SEJJ001). A.C. acknowledges financial support by the Swiss National Science Foundation. This research was undertaken thanks in part to funding from the Max Planck–University of British Columbia (UBC) Centre for Quantum Materials and the Canada First Research Excellence Fund, Quantum Materials and Future Technologies Program. The work at UBC was supported by the Killam, Alfred P. Sloan, and Natural Sciences and Engineering Research Council of Canada (NSERC) Steacie Memorial Fellowships (A.D.); the Alexander von Humboldt Fellowship (A.D.); the Canada Research Chairs Program (A.D.); the NSERC; the Canada Foundation for Innovation; and the Canadian Institute for Advanced Research Quantum Materials. The research leading to these results has received funding from LASERLAB-EUROPE (grant agreement no. 654148; European Union's Horizon 2020 research and innovation programme). The Y-Bi2212 crystal growth was performed in M.G.'s previous laboratory at Stanford University (Stanford, CA) and supported by the United States Department of Energy–Basic Energy Sciences. **Author contributions:** C.G., F.C., and F.P. conceived the experiments. C.G. coordinated the research activities with input from all the coauthors. The time-resolved x-ray photoemission setup at the Artemis facility was developed and coordinated by C.C., R.C., and E.S. The time-resolved photoemission measurements were performed by F.C., G.M., A.S., S.P., A.R., A.C., C.C., and C.G. The analysis of the time-resolved data was performed by F.C. and C.G., with particular input from M.C. The band structure calculations were carried out by M.B. Mean-field calculations of the oxygen band energy were performed by A.F.K. DMFT calculations were performed by M.C. The Y-Bi2212 crystals were grown and characterized by H.E., M.G., F.B., and A.D. The text was written by C.G. with major input from F.C., A.C., M.C., and F.P. All authors extensively discussed the results and the interpretation and revised the manuscript.
Competing interests: The authors declare that they have no competing interests.
Data and materials availability: All data needed to evaluate the conclusions in the paper are present in the paper and/or the Supplementary Materials. Additional data related to this paper may be requested from the authors.

Submitted 12 October 2017
Accepted 22 January 2018
Published 23 February 2018
10.1126/sciadv.aar1998

Citation: F. Cilento, G. Manzoni, A. Sterzi, S. Peli, A. Ronchi, A. Crepaldi, F. Boschini, C. Cacho, R. Chapman, E. Springate, H. Eisaki, M. Greven, M. Berciu, A. F. Kemper, A. Damascelli, M. Capone, C. Giannetti, F. Parmigiani, Dynamics of correlation-frozen antinodal quasiparticles in superconducting cuprates. *Sci. Adv.* **4**, eaar1998 (2018).

Downloaded from http://advances.sciencemag.org/ on August 16, 2018

Science Advances

Dynamics of correlation-frozen antinodal quasiparticles in superconducting cuprates

Federico Cilento, Giulia Manzoni, Andrea Sterzi, Simone Peli, Andrea Ronchi, Alberto Crepaldi, Fabio Boschini, Cephise Cacho, Richard Chapman, Emma Springate, Hiroshi Eisaki, Martin Greven, Mona Berciu, Alexander F. Kemper, Andrea Damascelli, Massimo Capone, Claudio Giannetti and Fulvio Parmigiani

Sci Adv **4** (2), eaar1998.
DOI: 10.1126/sciadv.aar1998

ARTICLE TOOLS http://advances.sciencemag.org/content/4/2/eaar1998

SUPPLEMENTARY MATERIALS http://advances.sciencemag.org/content/suppl/2018/02/16/4.2.eaar1998.DC1

REFERENCES This article cites 43 articles, 3 of which you can access for free
http://advances.sciencemag.org/content/4/2/eaar1998#BIBL

PERMISSIONS http://www.sciencemag.org/help/reprints-and-permissions

Use of this article is subject to the Terms of Service

Science Advances (ISSN 2375-2548) is published by the American Association for the Advancement of Science, 1200 New York Avenue NW, Washington, DC 20005. 2017 © The Authors, some rights reserved; exclusive licensee American Association for the Advancement of Science. No claim to original U.S. Government Works. The title *Science Advances* is a registered trademark of AAAS.

Downloaded from http://advances.sciencemag.org/ on August 16, 2018